GEOCHEMISTRY

Large sulfur isotope fractionation in lunar volcanic glasses reveals the magmatic differentiation and degassing of the Moon

Alberto E. Saal[1]* and Erik H. Hauri[2]

Sulfur isotope variations in mantle-derived lavas provide important constraints on the evolution of planetary bodies. Here, we report the first in situ measurements of sulfur isotope ratios dissolved in primitive volcanic glasses and olivine-hosted melt inclusions recovered from the Moon by the Apollo 15 and 17 missions. The new data reveal large variations in $^{34}S/^{32}S$ ratios, which positively correlates with sulfur and titanium contents within and between the distinct compositional groups of volcanic glasses analyzed. Our results uncover several magmatic events that fractionated the primordial sulfur isotope composition of the Moon: the segregation of the lunar core and the crystallization of the lunar magma ocean, which led to the formation of the heterogeneous sources of the lunar magmatism, followed by magma degassing during generation, transport, and eruption of the lunar lavas. Whether the Earth's and Moon's interiors share a common $^{34}S/^{32}S$ ratio remains a matter of debate.

INTRODUCTION

The extent, timing, and composition of lunar magmatism are fundamental pieces of information to understand the evolution of the Moon's interior. Two main types of lunar basalts have been studied: lava flows (i.e., mare basalts) and associated volcanic glass-rich pyroclastic deposits. Mare basalts and volcanic glasses define a large compositional range from high-Ti, to low-Ti, to very low–Ti magmas (1). Results from those studies inferred that the cooling and crystallization of the lunar magma ocean (LMO) created layered igneous cumulates and a late-stage layer component (urKREEP and ilmenite-rich) enriched in titanium and incompatible elements. Rayleigh-Taylor instabilities may have caused either the sinking of the late-stage dense layer that mixed with the earlier cumulates or a full overturn of the cumulate pile, generating the heterogeneous source region responsible for the compositionally diverse lunar volcanism (1).

The sulfur isotopes of the lunar magmatism provide fundamental insights into the thermal and compositional evolution of the Moon's interior: from the Moon-forming giant impact event, to core segregation and the crystallization of the LMO, to the processes responsible for the lunar magmas (2). The sulfur isotope composition of the Moon's interior is most directly reconstructed from the record preserved in the lunar mare basalts and pyroclastic deposits. However, this reconstruction is complicated by magmatic processes that modify the initial composition of the lavas (e.g., magmatic degassing and differentiation during transport and eruption, as well as magma interaction with shallow level reservoirs).

There have been considerable efforts to measure sulfur concentrations and $\delta^{34}S$ ($\delta^{34}S = [(^{34}S/^{32}S)_{sample}/(^{34}S/^{32}S)_{V-CDT} - 1] \times 1000$, where V-CDT is the Vienna-Canyon Diablo Troilite standard) in lunar samples returned by the Apollo missions (2–21). These studies found that lunar mare basalts, representing a range in major element compositions, have a remarkable uniform whole-rock acid-volatile (extraction with 3 M HCl) sulfur isotope ratios

with a mass-dependent mean isotopic composition of $\delta^{34}S = +0.58 \pm 0.05‰$ (2). This mean value is within the range measured for carbonaceous chondrites but is heavier than that reported for the Earth's mantle ($\delta^{34}S = -1.28 \pm 0.33‰$) (22), suggesting a different $\delta^{34}S$ value between the Earth's and Moon's interiors. A full compilation of mare basalt whole-rock $\delta^{34}S$ values, irrespective of the analytical technique used (different acid-volatile extraction, combustion in an oxygen atmosphere, or a combination of both), has a similar average but with a larger uncertainty ($\delta^{34}S = +0.47 \pm 1.5‰$, 2σ) (2, 6–12, 14, 15), yet part of the reported $\delta^{34}S$ range (2 to 2.5‰) could be caused by systematic analytical discrepancies between laboratories (6). These studies found a clear correlation between sulfur and titanium contents in mare basalts (5), and although never directly stated, the compiled published data on mare basalt hint to a correlation between titanium content and the $\delta^{34}S$ values.

In contrast to the mare basalts, reported bulk-sample $\delta^{34}S$ values of the lunar high-Ti volcanic glasses (74220 and drive tube 74001/2) range to significantly lighter values, with $\delta^{34}S$ from +0.69 to −2.6‰ (3, 4). These studies found that sulfur concentration increases and $\delta^{34}S$ values decrease with decreasing the grain size fraction of the sample analyzed (fig. S1) (4). They concluded that the unusual light $\delta^{34}S$ values of the volcanic glasses indicate the presence of a surface component produced by the condensation of a volcanic gas cloud onto the surface of the glass beads. Furthermore, they found that the sulfur concentration and $\delta^{34}S$ value of the sample decrease with increasing depth within the drive tube, suggesting more degassed volcanic glasses with depth. Two main factors have limited the interpretation of these data. First, the bulk-sample analysis makes it difficult to determine the contribution of the surface and the interior components to the total measured $\delta^{34}S$ value of the volcanic glasses. Second, the origin of the measured $\delta^{34}S$ is unclear. For example, a heavy $\delta^{34}S$ component was also measured during the bulk-sample analysis of some of the finest fractions and during leaching experiments of the high-Ti glasses (3, 4). The heavy $\delta^{34}S$ values indicate that the bulk-sample analysis had a fraction of mature regolith in it, whereas the leaching experiment points to the presence of a second surface component with heavy $\delta^{34}S$ (possibly due to interaction with the lunar regolith) on the glass surface (4).

[1]Department of Earth Environmental and Planetary Sciences, Brown University, Providence, RI 02912, USA. [2]The Earth and Planets Laboratory, Carnegie Institution for Sciences, Washington, DC 20015, USA.
*Corresponding author. Email: asaal@brown.edu

RESULTS

Here, using nanoscale secondary ion mass spectrometry (NanoSIMS) in situ analyses (*23*), we report the first $\delta^{34}S$ values measured in individual lunar volcanic glasses and olivine-hosted melt inclusions to evaluate the processes controlling their $\delta^{34}S$ variation. These samples, returned by the Apollo 15 and 17 missions, represent some of the best-studied and most primitive magmas generated from within the deepest regions of Moon (*1*). We measured $\delta^{34}S$ in the center of the exposed interiors of individual lunar volcanic glass beads and in olivine-hosted melt inclusions using a Cameca NanoSIMS 50L multicollector ion microprobe at the Carnegie Institution for Sciences (see Materials and Methods for a detailed description of the analytical techniques). The measured $\delta^{34}S$ value of the volcanic glass beads provides the isotopic composition of the magma at the time of fragmentation and eruption, before any interaction with the regolith and deposition of any surface coating. We examined three compositional groups: the very low– and low-Ti glasses from Apollo 15 (15426 and 15427) and the high-Ti glasses from Apollo 17 (74220). These glasses were previously characterized for major, trace, and highly volatile elements (*24*–*28*). Some olivine phenocrysts within the high-Ti glasses contain melt inclusions. These inclusions are small samples of magma trapped within the olivine that grew in the magma before eruption (*25*). Their $\delta^{34}S$ values and sulfur content are protected from modification by degassing and shallow-level contamination during eruption because of their enclosure within their host crystals. Thus, melt inclusions have the highest concentrations of sulfur, up to 884 parts per million (ppm), whereas the high-Ti glass beads contain 200 to 450 ppm sulfur. The low-Ti and very low–Ti glasses range from 250 to 750 ppm and 50 to 300 ppm sulfur, respectively. The $\delta^{34}S$ values vary from +1.3 to −1.8‰ in the high-Ti glasses, with their melt inclusions ranging from +1.6 to −0.30‰, whereas the $\delta^{34}S$ values of low- and very low–Ti glasses vary from −0.27 to −4.70‰ and from −4.80 to −14‰, respectively (Figs. 1 and 2 and table S1). Moreover, we report $\delta^{34}S$ values for four of the five subgroups of very low–Ti glasses defined by Delano (*29*) (A to E). These glasses define two separate arrays in Mg/Si ratios [weight % (wt %)]. A low-Mg/Si (A to C) and a high-Mg/Si (D and E) arrays, possibly produced by either magma mixing or assimilation of LMO cumulate during melt transport (*30*). Both arrays show essentially the same range in $\delta^{34}S$ values, and within each separate array, the $\delta^{34}S$ value decreases with decreasing Mg# (defined as $100 \times$ [MgO]/[FeO + MgO] in mol). Although we were not able to measure $\delta^{34}S$ in the compositional subgroup C, we expect it to be high in $\delta^{34}S$ due to its high Mg# and sulfur content (Fig. 3) (*20*, *24*, *29*).

Our new data in melt inclusions and volcanic glasses define a significant range in $\delta^{34}S$ and sulfur content within and among the three compositional groups. When combined with previously published geochemical data for lunar volcanic glasses (*24*–*28*), the $\delta^{34}S$ values define positive correlations with the sulfur content within each group and with the sulfur and titanium contents among the different compositional groups (Figs. 1 and 2). The $\delta^{34}S$ variation among the three groups is generally smaller than the internal variation within each group. Although correlation between sulfur and titanium contents in lunar basalts has been previously reported (*5*, *20*), our new data define a clear correlation between $\delta^{34}S$ values and titanium contents in lunar magmas (Fig. 2). These observations point to two main events that fractionated the $\delta^{34}S$ values of the lunar lavas. The first produced the difference in $\delta^{34}S$ among the different compositional groups, and the second caused the $\delta^{34}S$ values within each group.

DISCUSSION

Variations of $\delta^{34}S$ in volcanic rocks can be produced by both magmatic process and source composition variability. Thus, before the $\delta^{34}S$ value can be used as a source indicator for planetary sulfur, it is important to consider the magmatic processes that can change this value (*2*). Our data exhibit a positive correlation of $\delta^{34}S$ values with sulfur content within each compositional group (Fig. 1), a feature of the entire dataset independent of the compositional type of glass measured. This correlation points to a set of igneous processes that have modified the original $\delta^{34}S$ values in these lunar magmas during generation, transport, and eruption.

Solar wind implantation, gas condensation onto the surface of the volcanic glass bead, and cosmic ray spallation cannot be the source of the observed large $\delta^{34}S$ variation. The depth of implantation and gas condensation on the surface of the bead is ≤2 μ (*3*, *4*, *31*), but our in situ analyses are in the middle of glass beads, 70 to 240 μ from the bead surface (table S1). Although there are reports of possible spallation effect on $\delta^{33}S$ and $\delta^{36}S$ in lunar basalts, there is no observable effect on $\delta^{34}S$ (*2*). Furthermore, interaction of the volcanic glasses with the lunar regolith or impact blanket material during eruption is expected to increase the $\delta^{34}S$ value, without producing any correlation with the sulfur content. This is due to the enriched $\delta^{34}S$ values in the regolith and to a lesser extent in the breccias compared to those of lunar basalts at similar range of sulfur content (figs. S2 and S3). Therefore, other magmatic processes are likely responsible for the measured $\delta^{34}S$ variation within each of the lunar glass compositional groups.

Two main magmatic processes could modify the $\delta^{34}S$ value and sulfur contents in the lunar glasses: sulfide saturation/segregation and magma degassing.

The effect of sulfide saturation on $\delta^{34}S$ during the generation of the lunar magmas

Most experimental data suggest that lunar basalts were sulfide undersaturated during magma generation, transport, and eruption (*32*, *33*). Furthermore, based on the chalcophile and siderophile element contents of lunar basalts, it is unlikely that sulfide saturation and segregation took place during magma generation, cooling, and crystallization (*34*). However, new experimental work has challenged this conclusion (*35*). This study shows that the lunar basalt could have been saturated with an immiscible sulfide liquid having two components, Fe and FeS, during magma generation. It reveals a significant decrease in the sulfur content at sulfide saturation (SCSS) of the silicate melt because of the change in the activity of FeS component in the sulfide metal bleb as Fe saturation is approached at the fO_2 (oxygen fugacity) typical for the Moon interior (~1 log unit below iron-wüstite buffer fO_2 ~ ΔIW −1) (*1*). Therefore, whether sulfide saturation remained during lunar basalt generation and transport is debated; it depends critically on the initial sulfur content of the source and the extent of melting. We evaluate the effect that sulfide saturation would have on the sulfur content and the $\delta^{34}S$ value of the silicate melt and residue during basalt generation. We consider an initial sulfur content in the source of the lunar basalts of ~75 ppm (*27*), an extent of melting that ranges from 3 to 10% (*36*–*39*), and an fO_2 of ΔIW ~ −0.9, just before saturation with Fe metal. Using
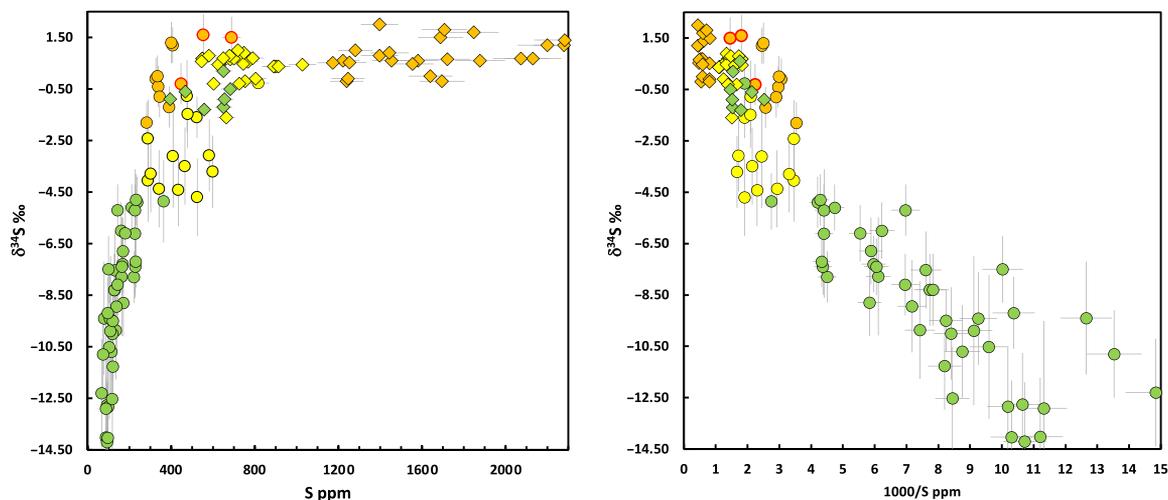
Fig. 1. δ^{34}S (‰) versus S content (ppm) and versus 1000/S (ppm^{-1}) in lunar basalts, analyzed by NanoSIMS. Note that δ^{34}S values positively correlate with the S content within each compositional group and between the different groups. Circles represent volcanic glasses and melt inclusions, whereas diamonds are mare basalts. Green, yellow, and orange colors indicate very low–, low-, and high-Ti compositions, respectively. Orange circles with red borders indicate melt inclusions from high-Ti volcanic glasses. Error bars represent SD (2σ) uncertainties. Data for the volcanic glasses are from this study and (24–28), and those for the mare basalt are from the literature (2, 6–12, 14, 15).
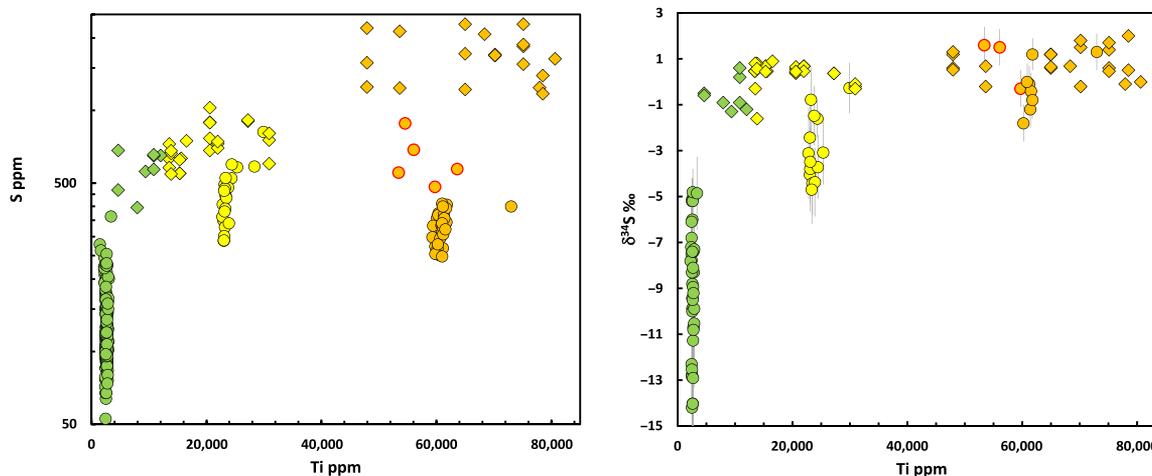

Fig. 2. Correlation among δ^{34}S (‰) and S and Ti contents (ppm) in lunar basalts. S content and δ^{34}S values versus Ti content for lunar basalts. Symbols and δ^{34}S and S data as in Fig. 1. Error bars represent SD (2σ) uncertainties. The Ti data for the volcanic glasses are from (24–28), and those for mare basalts are compiled from https://curator.jsc.nasa.gov/lunar/lsc/index.cfm.

the Brenan *et al.* (35) model, the SCSS in the silicate melt will be approximately 1550 ppm at 2 GPa and 1450°C, within the range proposed for the generation of the lunar volcanic glasses [see compilation in (33)]. Under the restrictions of these initial conditions, the sulfide is exhausted as a residual phase after ~5% melting. We do not expect substantial changes in the major element composition of the melts generated between 1 and 5% melt fraction to significantly affect the SCSS, and therefore, the sulfur content of the silicate melt will remain relatively constant at ~1500 ppm as long as sulfide remains as a residual phase. In contrast, the δ^{34}S value of both the residue and silicate melt is expected to change during melting. At the reducing conditions of the lunar magmas (f_{O_2} ΔIW ~ 0 to −2), the sulfur species dissolved in the silicate melt is only S^{2-} (40). The expected equilibrium isotope fractionation factor between

S^{2-} in the silicate melt and FeS [$\alpha_{melt-FeS}$ = (^{34}S/^{32}S)$_{melt}$/(^{34}S/^{32}S)$_{FeS}$] will range from 0.999 to 0.998 at 1450°C (section S1) (41). Note that

$$\delta^{34}S_{melt} - \delta^{34}S_{FeS} = \Delta^{34}S^{melt-FeS} = 1000(\alpha_{melt-FeS} - 1) \approx 1000\ln\alpha_{melt-FeS} \quad (1)$$

The expected variation of δ^{34}S in the melt over ~5% melting would range by ≤2‰ for equilibrium to ≤7‰ for fractional melting before sulfide exhaustion (table S2). The model data suggest that the δ^{34}S value increases, whereas the sulfur content of the melt remains nearly constant with increasing extent of melting. This model fails to explain the positive correlation between δ^{34}S values and sulfur contents within each compositional group of lunar glasses. Moreover, we would expect an inverse correlation between δ^{34}S and very
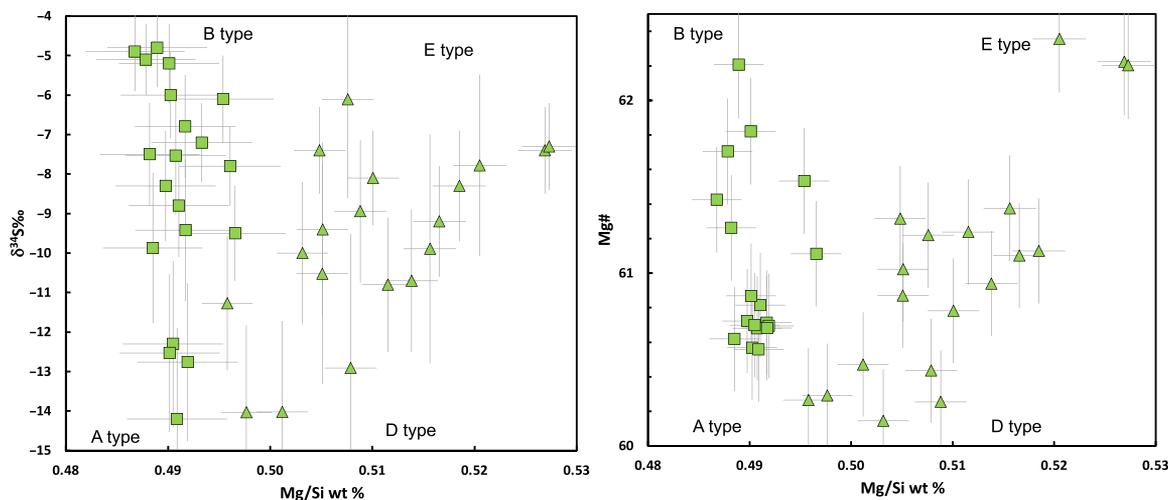
Fig. 3. δ^{34}S (‰) and Mg# versus Mg/Si (wt %) for the very low–Ti volcanic glasses. The five subgroups of very low–Ti glasses define two separate arrays low-Mg/Si (green squares; subgroups A, B, and C) and high-Mg/Si (green triangle; subgroups D and E). Data compilation from this study and (*24–28*). Mg# = 100 × [MgO/(FeO + MgO)] (mol). Error bars represent SD (2σ) uncertainties. We were not able to measure δ^{34}S in subgroup C, but we expect it to be high in δ^{34}S as it has high Mg# and higher volatile contents (*20, 24, 29*).

incompatible element contents (e.g., cerium) in the melt with increasing extent of melting, which is not observed in our data. Although sulfide saturation during melt generation might have occurred, this was not the main process controlling the δ^{34}S variation within each compositional group of lunar volcanic glasses.

The effect of magmatic degassing

Magmatic degassing is the most likely mechanism responsible for the observed covariation of δ^{34}S values and sulfur contents within the compositional groups of volcanic glasses. Several lines of evidence from previously published data support this inference: (i) Bulk-sample analyses of high-Ti glasses show an increase in sulfur concentration and a decrease in δ^{34}S value with decreasing of the grain size fraction analyzed (fig. S1) (*3, 4*). These results were interpreted as evidence for the presence of a surface component with light δ^{34}S values produced by the condensation of the volcanic gas cloud onto the volcanic bead surface. These correlations are opposite to those defined by the lunar regolith, where the δ^{34}S value and the sulfur content increase as the grain size fraction analyzed decreases (fig. S3) (*3*). (ii) Recent whole-rock analyses of four mare basalts with δ^{34}S values below the lunar average +0.58 ± 0.05‰ are consistent with 40 to 60% degassing of a H_2S ± COS bearing gas (*2*). (iii) We observed correlations between the new δ^{34}S values and the volatile contents within and between the three compositional group of volcanic glasses (Figs. 4 and 5) (*24–28*). The best example is the high-Ti glasses, because data exist not only for the glasses but also for the olivine-hosted melt inclusions. These correlations are progressively less clear in the following order: S, F, Cl, H, and C contents. Two processes control the magmatic degassing of the lunar volcanic glasses: equilibrium degassing (close and/or open system) during melt transport and kinetic processes during bubble formation, melt fragmentation, and eruption (*28*). Not only the solubility of H and C species is much lower in basaltic melts but also their diffusivities are higher than those of Cl, F, and S, where F and S have the lowest diffusion coefficients (*24–28*). Thus, better correlations are found between δ^{34}S and S, and progressively less well-defined trends are observed with F, Cl, H, and C contents,

which are increasingly more affected by degassing and kinetic processes (Fig. 2).

Here, we present a simple equilibrium open-system degassing model (*41*) for the lunar volcanic glasses and evaluate the effect of kinetic isotope fractionation due to diffusive transport of sulfur in the melt and evaporation/condensation processes. We consider open-system degassing consistent with the low viscosity of the melt, which allowed gas segregation during transport and eruption of the lunar volcanic glasses (*42*). The δ^{34}S values and the volatile contents of the different compositional groups of glasses point to different initial δ^{34}S values and S, F contents that have not been completely erased by degassing during melt transport and eruption (Figs. 4 and 5). We considered three different initial sulfur contents and δ^{34}S values based on the highest measured data for each compositional group, where the δ^{34}S value and the sulfur content decrease with decreasing titanium content. Thus, we estimated initial sulfur content of 900, 800, and 700 ppm and δ^{34}S values of +1.7, 0, and −1.5‰ for the high-, low-, and very low–Ti glasses, respectively. The most uncertain initial values are related to the very low–Ti glasses. The sulfur content was obtained from bulk-sample glass analyses (*43*), and δ^{34}S was assumed on the basis of the measured values for the very low–Ti glasses and mare basalts.

We used published experimental data (*23, 41, 44*) and thermochemical model (*45*) to estimate the equilibrium isotope fractionation factor $\alpha_{gas-melt}$ at a pressure and temperature range of 10^3 to 1 bar and 1300° to 1000°C and reducing conditions (fO_2 ΔIW ~ −1) relevant to lunar magmas (section S2). Under these conditions, the sulfur species in the silicate melt is S^{2-} (*40*), and the coexisting major sulfur species in the gas are H_2S, COS, and S_2 (*45*). Depending on the pressure-temperature-fO_2 path of the melt gas, the proportion of H_2S + COS ranges between 94 and 37% of the total sulfur in the gas, whereas S_2 varies from 6 to 63% (*45*). Combining the proportions of the gas species with the estimated equilibrium fractionation factor between the silicate melt and pure gas specie (table S3), we obtain a range in $\alpha_{gas-melt}$ from 1.0016 to 1.0042. In our model, for simplicity, we used a constant $\alpha_{gas-melt}$ with an intermediate value of 1.003. Clearly, this is an oversimplification of the problem, given
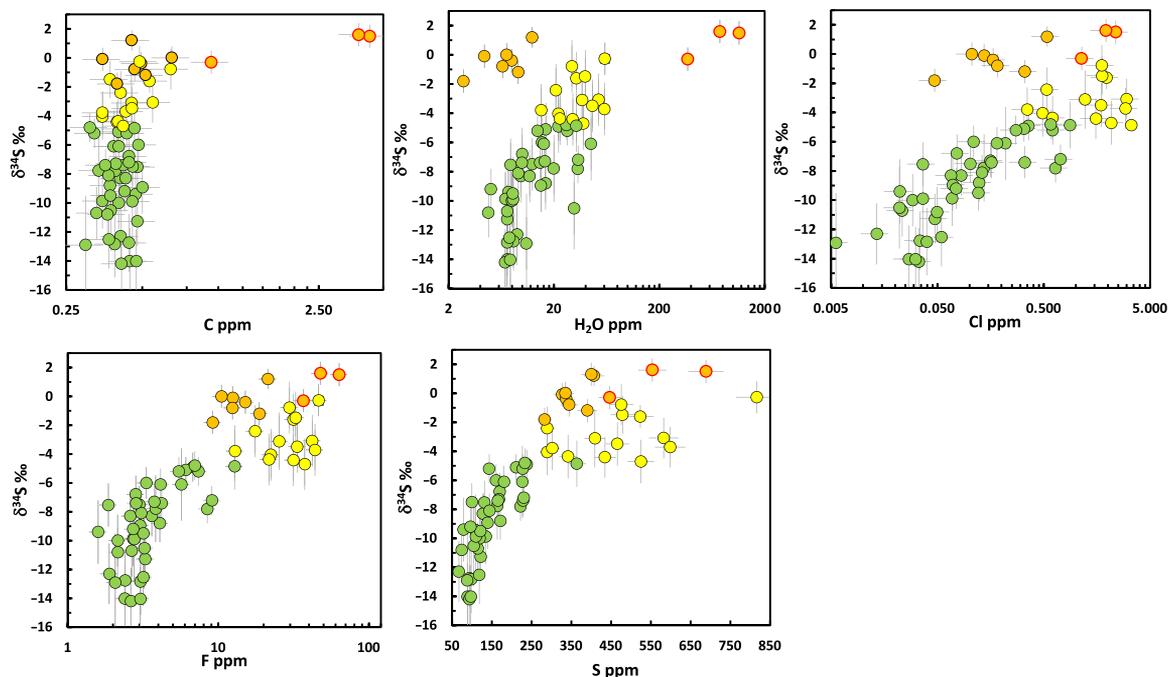
Fig. 4. δ^{34}S (‰) versus highly volatile element contents (ppm) of lunar glasses. δ^{34}S positively correlates with the volatile content within each compositional group and among the different groups. The poor correlations with H_2O and C compared to those with Cl, F, and S contents indicate that equilibrium degassing and kinetic processes significantly affected the initial H_2O and C concentrations of the basalts but did not completely erase the initial differences in S, F, and Cl contents among the distinctive compositional groups. Error bars represent SD (2σ) uncertainties. Data compilation from this study and (24–28). Symbols as in Fig. 1.
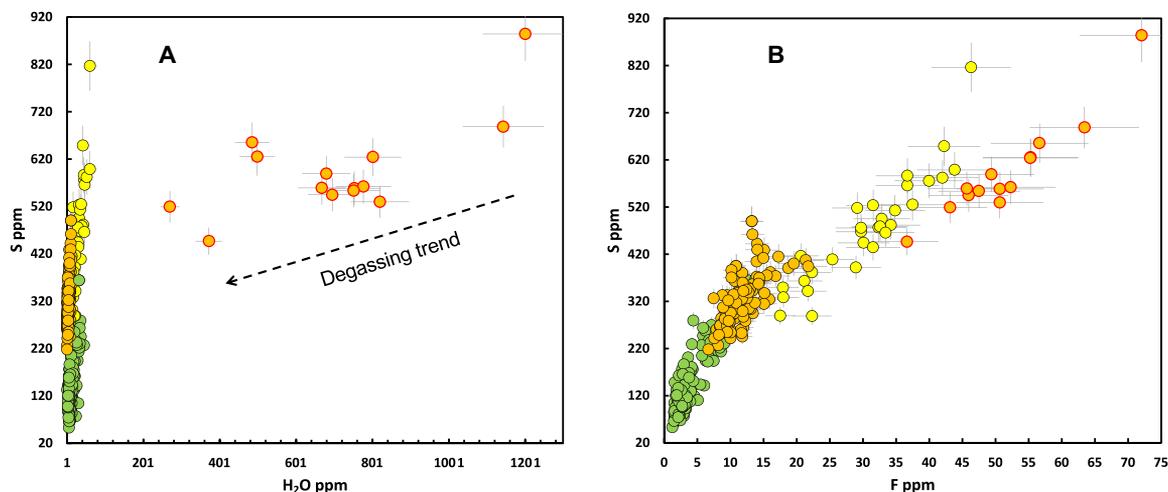

Fig. 5. S, H_2O, and F contents (ppm) in volcanic glasses. (**A**) S versus H_2O, and (**B**) S versus F for the lunar glasses and melt inclusions. Symbols as in Fig. 1. The two panels show the different effect that magmatic degassing had on H_2O relative to F and S contents. Error bars represent SD (2σ) uncertainties. Although the initial differences in H_2O and C among the different compositional groups of glasses have been erased by magmatic degassing, the initial differences in S, F (and to a lesser extent Cl) contents among the three compositional groups still remain. This is due to the lower effect that magmatic degassing has on the latter elements (see also Fig. 4). Data from (24–28). Symbols as in Fig. 1.

that the $\alpha_{gas\text{-}melt}$ will change with the pressure-temperature-f_{O_2} path during melt transport and degassing. However, the simple model reproduces the first-order variation of the measured data (Fig. 6). A more complicated model is unwarranted given the analytical uncertainty, the lack of experimental data on $\alpha_{gas\text{-}melt}$, and the changes of gas speciation in equilibrium with the melt as pressure, temperature, and f_{O_2} change during melt degassing.

Previous works have shown that single lunar glass beads have core-rim diffusion profiles for sulfur and other volatiles (24, 28). This suggests possible diffusion-limited kinetic isotope fractionation in a low-pressure environment following fragmentation of the magma during eruption (26). Therefore, it is important to consider how sulfur diffusion in the melt might affect the ^{34}S/^{32}S ratios of the magmatic sulfur contained in lunar volcanic glasses.

The mass dependence of diffusion of sulfur isotopes can be represented as

$$\frac{D^{32}S}{D^{34}S} = \left(\frac{m_{34_S}}{m_{32_S}}\right)^{\beta_{32_S/34_S}} \quad (2)$$

where D is the diffusion coefficient, m is the atomic or molecular mass of the diffusing species, and β is an empirical exponent that likely depends on sulfur speciation (40). In silicate melts and glasses, the value of β is generally found to be <0.5 and is correlated with the diffusivity of the element (46, 47). For ions with small diffusivity, i.e., similar to that of the ions that form the polymerized silicate network, the value of β is small, ~0.05. Ions that diffuse more rapidly than silicate network formers have larger values of β, increasing toward 0.5 as the diffusivity becomes large. The explanation that has been put forward to justify this correlation is that slow diffusion ions are strongly coupled to the motion of the silicate network such that a large number of atoms must move in concert to allow these ions to diffuse (46, 47). The involvement of the other atoms reduces the isotopic mass dependence. On the basis of the empirical relationship between the diffusivity of a species and its isotope mass dependence (46), we used the experimentally determined diffusivity of sulfur ~1.76×10^{11} m^2/s (20, 48) and SiO$_2$ ~ 4.55×10^{11} m^2/s (49) in lunar basalts at 1400°C to obtain a very small value of β ~ 0.015 (46), which suggests very limited kinetic fractionation. The near-zero value for β has been supported with recent experimental data for diffusion of sulfur isotopes in basaltic melts at 1350° to 1500°C and 1 to 1.5 GPa (50). Therefore, we do not expect significant fractionation of sulfur isotopes due to sulfur diffusion within the melt.

Kinetic isotopic fraction during evaporation and condensation at the surface of the volcanic melt is another possible process that might affect the δ^{34}S values of the lunar volcanic glasses (51, 52). The kinetic isotope fractionation depends on the degree of super/undersaturation of the gas medium surrounding the melt. The assumptions in the simplified approach taken here are as follows: (i) The melt during evaporation, and gas during condensation, remains homogeneous and well mixed; (ii) the isotopes of the same element have the same evaporation/condensation coefficients (i.e.,

$\gamma^{34}S = \gamma^{32}S$); and (iii) the coefficient of evaporation and condensation is equal as P/P_{sat} tends to 1, where P is the pressure of the evaporating species at the surface of the melt and P_{sat} is the saturation vapor pressure. When both equilibrium and kinetic isotope fractionation are taken into account during evaporation and condensation (52), the equations can be expressed by

$$\Delta^{34}S_{Evaporation}^{melt-gas} = \Delta^{34}S_{Equilibrium}^{melt-gas} - \left(1 - \frac{P}{P_{sat}}\right)\Delta^{34}S_{Kinetic} \quad (3)$$

$$\Delta^{34}S_{Condensation}^{solid-gas} = \frac{P_{sat}}{P}\Delta^{34}S_{Equilibrium}^{solid-gas} + \left(1 - \frac{P_{sat}}{P}\right)\Delta^{34}S_{Kinetic} \quad (4)$$

where

$$\Delta^{34}S_{Kinetic} = 1000\left(\frac{\gamma_{34_S}}{\gamma_{32_S}}\sqrt{\frac{m_{32_S}}{m_{34_S}}} - 1\right) \quad (5)$$

We used the previously estimated $\alpha_{gas-melt}$ of 1.003 during equilibrium magmatic degassing to obtain a $\Delta^{34}S_{Equilibrium}^{melt-gas}$ of −3‰. The $\Delta^{34}S_{Kinetic}$ ranges from −29 to −16.5 to −15‰ considering H$_2$S, COS, and S$_2$ as the gas species present, respectively. When we take into consideration the proportion of the different gas species (45), we obtain an intermediate $\Delta^{34}S_{Kinetic}$ of ~−22‰ (section S2). The calculated $\Delta^{34}S_{Evaporation}^{melt-gas}$ over a range of P/P_{sat} from 1 to 0 (table S4) demonstrates that significant kinetic isotope fractionation during evaporation would produce a trend of increasingly heavy δ^{34}S values with decreasing sulfur contents in the melt—a trend that is the opposite to that defined by the volcanic glass data. Only when P/P_{sat} closely approaches 1 (i.e., >>0.9), the model would be consistent with the data, suggesting that kinetic isotope fractionation of sulfur during evaporation was not a significant factor. This is also consistent with the lack of correlation between δ^{34}S and bead size (ranging from 140 to 480 μ; table S1) and the very limited core-rim diffusion profiles for sulfur in single lunar glass beads (24).

In the case of condensation, we considered two possible condensing species from the gas ZnS and native sulfur (53) and the proportion of H$_2$S, COS, and S$_2$ in the gas at a range of pressure, temperature, and f_{O_2} from 1 to 10^{-2} bar, 1300° to 700°C, and IW to IW-2 (41, 45), respectively. We estimated a range in $\Delta^{34}S_{Equilibrium}^{solid-gas}$ from 0 to 0.4 ‰
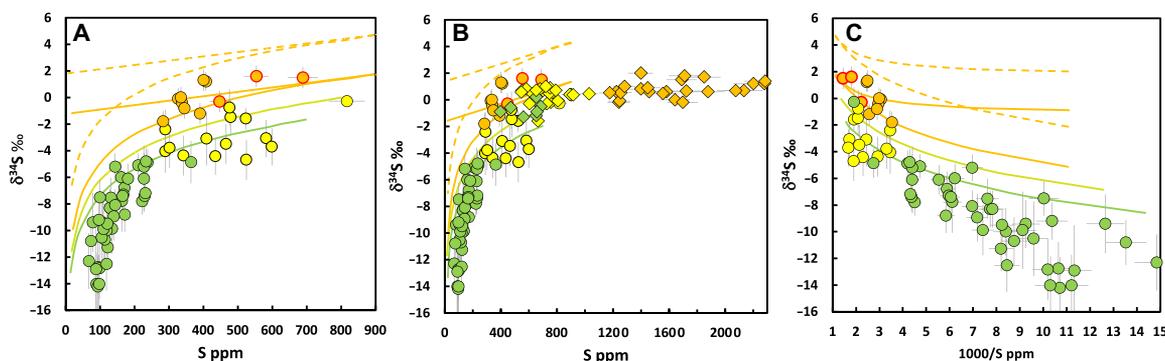

Fig. 6. Model of magmatic degassing for the lunar volcanic glasses. (A and **B)** δ^{34}S (‰) versus S content (ppm) for the volcanic glasses without and with the mare basalts, respectively. **(C)** δ^{34}S (‰) versus 1000/S (ppm^{-1}) for volcanic glasses. Error bars represent SD (2σ) uncertainties. Full lines indicate the model for the evolution of the melt during open-system degassing. Green, yellow, and orange colors denote the expected degassing trend for the very low–, low-, and high-Ti glass compositions, respectively. Closed-system degassing is only shown for the high-Ti glasses for clarity. Orange dashed curves represent the evolution of the gas composition during closed- and open-system degassing of the high-Ti glasses. Note in (C) that the very low–Ti glass data define almost linear trend δ^{34}S versus 1000/S progressively deviating from the degassing model with decreasing S contents. This is consistent with the hypothesis that magma mixing is partially responsible for the geochemical variation measured in very low–Ti glasses (30) Symbols and data as in Fig. 1.

(with an average of 0.15‰), indicating very limited equilibrium isotope fractionation between condensates and gas (table S3). In contrast, we estimate a large $\Delta^{34}S_{Kinetic}$ of −10 and −30‰ for ZnS and S, respectively. The calculated $\Delta^{34}S_{Condensation}^{solid-gas}$ over a range of P_{sat}/P from 1 to 0 (table S4) indicates that significant kinetic isotope fractionation should occur during condensation, producing the deposition of light $\delta^{34}S$ condensates on the surface of the volcanic glass beads. These results are consistent with the inferred light $\delta^{34}S$ values of the surface-correlated sulfur content of the high-Ti volcanic glasses (fig. S1) (3, 4).

An important feature of the data is the decreasing initial $\delta^{34}S$ and sulfur values with decreasing titanium content for the three compositional groups of volcanic glasses analyzed (Figs. 1 and 2). This observation is consistent with the generation of the lunar basalts during melting of a heterogeneous LMO cumulate pile. The heterogeneous sources of the diverse lunar magmatism were produced by admixtures of early cumulates with variable amounts of ilmenite and urKREEP components generated during the latest stages of LMO crystallization (1).

The very low–Ti volcanic glasses with depleted trace elements and volatile contents, including low sulfur, most likely represent melts from the early LMO cumulate that did not interact with the late-stage ilmenite and urKREEP components (1). Therefore, these glasses might provide clues to the LMO's $\delta^{34}S$ values at the time of cumulate formation. The light $\delta^{34}S$ values of these glasses suggest an initial $\delta^{34}S$ −1 to −1.5‰, lower than the values for chondrites ~0‰ but similar to the reported $\delta^{34}S$ of the Earth's mantle ($\delta^{34}S$ = −1.28 ± 0.33‰) (22). One possible explanation is that the Moon-forming impact event did not significantly affect the sulfur isotopes, and the Moon as well as the LMO early formed cumulates inherited the light sulfur isotopes from the Earth's mantle. Another possible interpretation is that the bulk Moon started with a chondritic sulfur isotope or even slightly heavier $\delta^{34}S$ value (2), but significant fraction of the initial sulfur was sequestered during core formation producing a light $\delta^{34}S$ value for the LMO.

We evaluate whether core segregation could produce a light $\delta^{34}S$ value in the LMO using a similar approach used to explain the light $\delta^{34}S$ of the Earth's mantle (22). Several lines of evidence from geophysical studies (e.g., seismology and core dynamo), to geochemical analyses of the chalcophile and siderophile elements in lunar basalts, to experimental reports on phase equilibria on possible core compositions at the relevant pressure and temperature conditions have been used to define the size and composition of the lunar core (54–56). These investigations suggest a lunar core of ~1 to 2.5 mass %, with low sulfur content of ~1 to 2 wt %. We considered for our model a core mass fraction in the range of 2 mass %, an initial bulk Moon sulfur content of 250 ppm, equivalent to that of the bulk silicate Earth (57), with a chondritic $\delta^{34}S$ = 0 ‰, and a metal-silicate melt sulfur partition coefficient of ~100 (58, 59). Under the restrictions of these initial conditions and considering batch equilibrium as well as open-system sulfur incorporation into the core, a $\delta^{34}S$ value within −1 to −1.5‰ for the LMO implies (i) a final bulk silicate Moon with 83- to 33-ppm S, which is comparable to estimates based on the geochemistry of lunar basalts (27); (ii) a moon core sulfur content of 0.8 to 1.1 wt %, consistent with geochemical and geophysical observations (54–56); and (iii) a sulfur isotope fractionation factor $\alpha_{core-LMO}$ value of 1.0016 to 1.0007, values within the range of the limited experimental data available (60, 61). Therefore, all geochemical and geophysical observations are consistent with

the hypothesis that the light $\delta^{34}S$ of the very low–Ti volcanic glasses could have been produced by the Moon's core segregation (Fig. 7).

In contrast, the high-Ti volcanic glasses with enriched trace elements and volatile contents, including high initial sulfur content and $\delta^{34}S$ +0.8 to +1.6‰, point to a component generated during the late-stage crystallization of the LMO. The crystallization of the LMO will generate a late-stage ilmenite and urKREEP components enriched in incompatible elements and volatile contents, including S, which most likely reached sulfide saturation (34). Therefore, the addition of these late-stage components to the early LMO cumulate pile would increase the sulfur and $\delta^{34}S$ values, as well as the titanium content, giving rise to the source of the high-Ti lunar magmas (1).

We evaluate the effect that sulfide saturation had on the $\delta^{34}S$ value of the cumulates formed during the late stages of the LMO crystallization. Most models agree that by the end of the LMO crystallization (≥90%), the residual melt reached sulfide saturation (34). We use Ding et al. (33) model to determine the SCSS, and the reported major element composition and sulfur content of the urKREEP (62) representing the residual melt after ≥90% crystallization. We considered a pressure from 0.2 to 0.6 GPa, given that the base of the anorthosite crust would be 34 to 43 km (~0.14 to 0.18 GPa) (63), a temperature of 1000°C, and an fO_2 ~ ΔIW −1 (64). Moreover, we assumed that the sulfide composition ranged between pure troilite and FeS with 10% Ni. Under these conditions, the SCSS for the silicate melt will range from 549- to 611-ppm sulfur, significantly below the estimated ~1220-ppm sulfur of the urKREEP. Our results are consistent with the hypothesis that the late-stage crystallization of the LMO reached sulfide saturation (34). We estimated a range in the FeS-silicate melt equilibrium isotope fractionation factor $\alpha_{FeS-melt}$
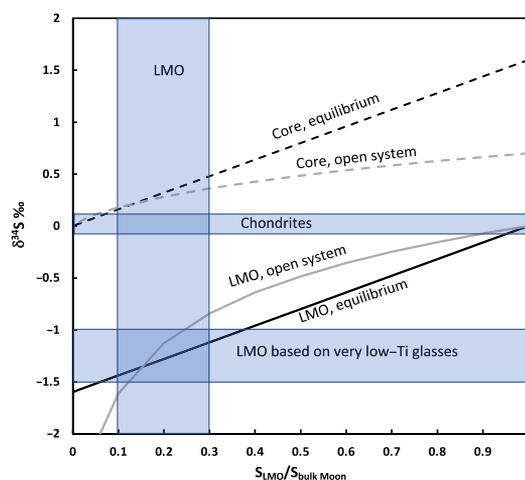

Fig. 7. Core-LMO sulfur partitioning model in batch equilibrium or open system. The $\delta^{34}S$ values (‰) of the LMO and lunar core are plotted against the ratio of the sulfur content of LMO during core segregation to that of the bulk Moon. In the open-system model, the core is treated as a cumulative product. We considered for our model a core mass fraction in the range of 2 mass % (54–56), an initial bulk Moon sulfur content of 250 ppm, with a chondritic $\delta^{34}S$ = 0 ‰ (34), and a metal-silicate melt sulfur partition coefficient of ~100. The model indicates that if the LMO reaches a range in $\delta^{34}S$ between −1 and −1.5‰ after core segregation, it will result in an LMO sulfur content between 83 and 33 ppm, a core S content of 0.8 and 1.1 wt %, and an equilibrium sulfur isotope fractionation factor $\alpha_{core-mantle}$ of 1.0016 and 1.0007 for batch equilibrium and open system, respectively. All output results are within values previously estimated or experimentally determined (34, 54–56, 60, 61).

of 1.004 and 1.002 at 1000°C (see table S3) (*41*, *44*). In our model, we used an intermediate $\alpha_{FeS-melt}$ of 1.003 and a range for the initial $\delta^{34}S$ values of the LMO after core segregation from −1.5 to −1‰ (Fig. 7). A simple closed-system crystallization of the urKREEP suggests that cumulates formed by up to ~40% crystallization will have $\delta^{34}S$ values ranging from +0.3 to +1.5‰ and from +0.8 to +2‰, depending on the initial $\delta^{34}S$ of the LMO, respectively. These values are consistent with the expected cumulate layer that gave origin to the high-Ti lunar lavas with $\delta^{34}S$ +0.5 to +1.6‰. The sinking of the late-stage dense (urKREEP-ilmenite–rich) layer and the variable mixing with the earlier LMO cumulates will create variable source compositions, providing a reasonable explanation for the increasing initial $\delta^{34}S$ and sulfur values with increasing titanium content of the three compositional groups of lunar volcanic glasses.

Although the heterogeneous LMO cumulate pile can explain the sulfur and $\delta^{34}S$ variation among different compositional groups, there are differences between mare and volcanic glasses within a single compositional group (e.g., high-Ti basalts) that are harder to explain. For example, the $\delta^{34}S$ value in the high-Ti mare basalts remains relatively constant, while the sulfur content varies by 50% (*2*), whereas the $\delta^{34}S$ value in the high-Ti volcanic glasses change by ~4‰ over an equivalent variation in sulfur content. This difference points to distinct source compositions (e.g., proportion of urKREEP-ilmenite–rich component) and/or conditions (pressure, temperature, and fO_2) of melt generation, melt transport, and eruption. How those differences affected sulfide saturation and sulfur degassing of the magmas and consequently their final sulfur content and $\delta^{34}S$ values remains a matter of debate.

Our new data show that the $\delta^{34}S$ variability in lunar volcanic glasses is similar to that previously reported for $\delta^{37}Cl$ and $\delta^{66}Zn$ values (*65*, *66*) and most likely associated to magmatic degassing. Several lines of evidence point to magmatic degassing as the main factor controlling not only $\delta^{37}Cl$ and $\delta^{34}S$ [(*65*) and this study] but also $\delta^{66}Zn$: (i) The analyses of high-Ti glasses (74220 and drive tube 74001/2) show that the variations in zinc content and $\delta^{66}Zn$ values with the grain size fraction analyzed and with depth within the drive tube mirror the variations in sulfur contents and $\delta^{34}S$ values (figs. S1 and S4) (*3*, *4*, *67*). These correlations suggest that zinc and sulfur have been affected by magmatic degassing and later condensation of the volcanic gas cloud onto the surface of the volcanic glass beads. (ii) Detailed petrological study of Mg-suite and ferroan anorthosite lithologies in breccia sample 67016 and 67915 display evidence of sulfurization due to interaction with a magmatic sulfur-rich vapor (*68–70*). The sulfurization features are restricted to individual clasts, do not cut across the matrix surrounding the clasts, and therefore predate the breccia-forming event. The in situ SIMS analyses of the vein and replacement troilite within the clasts have light $\delta^{34}S$ values from −1.0 to −3.3‰, consistent with the whole-rock $\delta^{34}S$ of −3.4‰. In contrast, the matrix surrounding the clasts has a whole-rock $\delta^{34}S$ of 0‰ (*69–70*). If we consider that the $\delta^{34}S$ values of the replacement troilite were produced at temperature of 700°C (*70*) and use the corresponding equilibrium isotope fractionation $\alpha_{FeS-H2S} \sim 1.00026$ between sulfide and H_2S magmatic gas (see table S3) (*71*), it will indicate a S-rich magmatic vapor with $\delta^{34}S$ values ranging from −1.3 to −3.6‰. This range is consistent with a magmatic vapor, produced by open-system degassing, in equilibrium with the $\delta^{34}S$ values of the volcanic glasses reported in this study. The brecciated anorthosite sample 67955, which comes from the same small boulder as sample 67915, has high zinc content ~6 ppm

and very light $\delta^{66}Zn$ value −6.98‰ (*66*), mimicking the sulfur content an $\delta^{34}S$ in sample 67915. These observations suggest that both $\delta^{34}S$ and $\delta^{66}Zn$ values were related to a single process: the interactions between the early formed lunar crustal rocks and a latter high temperature vapor phase rich in light sulfur and zinc isotopes. Previous studies interpreted the light $\delta^{66}Zn$ in sample 67955 and in few other brecciated anorthosites to be driven by vaporization of an impact blanket (*66*). Several observations based on the sulfur data point to a magmatic, rather than impact, origin of the vapor. First, the correlation between $\delta^{66}Zn$ and $\delta^{34}S$ with grain size in the high-Ti volcanic glasses indicates condensation of a magmatic vapor with light $\delta^{66}Zn$ and $\delta^{34}S$ values. Second, the sulfurization process, which produced the light $\delta^{34}S$ isotope in sample 67915, is in the clasts rather than the matrix of the breccia. Third, approximately 30 breccias and impacted lunar rocks have been analyzed for $\delta^{34}S$, with ~90% of them showing heavy rather than light sulfur isotopes (fig. S2), suggesting that the impact processes might not be the source of the light $\delta^{34}S$ vapor phase. Therefore, it seems more likely that the ferroan anorthosite and Mg-suite plutonic rocks with light $\delta^{66}Zn$ and $\delta^{34}S$ values represent early lunar crust affected by percolating gas/fluids associated to a latter basaltic magmatism.

In summary, core segregation, LMO crystallization, and finally magmatic degassing during basalt generation, transport, and eruption have extensively modified the primordial sulfur isotope composition of the Moon; thus, estimations on the $\delta^{34}S$ value of the bulk silicate Moon are uncertain and model dependent. Therefore, whether the Earth's and Moon's interiors share a common $\delta^{34}S$ remains a matter of debate.

MATERIALS AND METHODS

We used a Cameca NanoSIMS 50L multicollector ion microprobe at the Carnegie Institution for Science to measure the $^{34}S/^{32}S$ ratios in the center of exposed sections of individual lunar olivine-hosted melt inclusions and volcanic glass beads from samples 74220, 15426, and 15427 (table S1). The glasses and melt inclusions were previously analyzed for major, trace, and volatile contents and hydrogen isotopes (*24–28*). The in situ measurements of the interiors of individual volcanic glass beads and inclusions, far removed from surfaces containing implanted solar wind, avoid terrestrial and solar contamination. The method of high-precision in situ SIMS analysis of sulfur isotopes in glasses down to a few hundreds of ppm of bulk sulfur has been previously established (*23*, *44*, *72*, *73*). They demonstrated that the effects of varying bulk composition (major elements, water and sulfur contents) and oxidation states are negligible and do not influence instrumental mass fractionation. For the analyses reported here, our analytical methods follow routines previously described (*23–26*, *73*). We obtained data in two different modes of SIMS operation: standard dynamic SIMS and scanning ion imaging SIMS. Analysis of glass beads was performed using standard dynamic SIMS, whereas the measurements of 74220 olivine-hosted melt inclusions were performed only with Scanning Ion Imaging SIMS. The errors in $^{34}S/^{32}S$ ratios measured by dynamic and scanning ion imaging SIMS were propagated by taking the square root of the sums of the 2-sigma analytical errors for unknowns and uncertainty in the standard values. The sulfur background measurements using Suprasil and Herasil silica glasses within the sample mounts ranged from 0.06 to 0.3 ppm, making background correction unnecessary.

Dynamic SIMS

In this mode of operation, only ion counts are recorded as data with no associated imaging. We tuned the mass spectrometer for a mass resolving power of ~6000 Mass Resolving Power (MRP), sufficient to resolve oxygen dimers from sulfur masses, $^{31}P^1H$ from ^{32}S, and $^{32}S^1H_2$ and $^{33}S^1H$ from ^{34}S. A typical ~15-min measurement used a Cs+ primary beam of 2 nA, accelerated to 8 kV and 2 μm diameter with collection of negatively charged secondary ions. A normal incidence electron gun was used to compensate excess charge. For each analysis, we first performed a pre-sputtering routine with the primary beam rastered over a 25 μm by 25 μm area for 3 min to remove the gold coat and sputter through the surface layer. During this time, we monitored secondary ion images of ^{12}C and ^{32}S to avoid cracks that appear as bright features on the projected ^{12}C image and dendritic crystals that appear as dark features on the projected ^{32}S image. The pre-sputter was followed by a reduction in the raster size to 20 μm by 20 μm divided into regions of 64 × 64 pixels with 245-μs dwell time per pixel on each pixel (equivalent to ~1 s/frame) with simultaneous acquisition of data for ^{12}C ^{18}O ^{32}S ^{34}S in multicollection mode. Counting times were 1 s for all masses, and we collected 600 ratios (600 s total counting time). The average run precision is ±1.5‰, with a range from ±0.7 to ±3.5‰ (2σ) that roughly inversely correlates with sulfur concentration. Pressure in the ion probe sample chamber was ~6 × 10^{-10} torr during the analyses. We analyzed the basaltic glass standard after every two to three analyses of lunar glass beads to continuously monitor the instrumental drift and mass fractionation (IMF) of sulfur isotopes. Measured sulfur isotope ratios were corrected for the long-term analytical drift of the instrumental fractionation using a time-based linear interpolation of all $^{34}S/^{32}S$ values of the standard glass ET83viii (23, 44, 72) analyzed within each analytical session (fig. S5A). Under these conditions, typical count rates on standard glass ET83viii (919-ppm S) were ~450,000 counts per second (cps) for ^{32}S and ~20,000 cps for ^{34}S. The IMF factor [αSIMS = ($^{34}S/^{32}S$meas)/($^{34}S/^{32}S$true)] measured from session to session ranges from 1.013 to 1.039. Changes in IMF during SIMS analyses can be related to changes in instrumental tuning conditions and properties of the mounts used to hold the samples. As a result, boundaries between blocks of data within analytical sessions were defined by any one of the following: (i) changing of the sample mount, (ii) changes to electron multiplier (EM) high voltage (gain), (iii) adjustments in primary beam intensity >20%, and (iv) any major retuning of the primary or secondary optics or electron gun. In all cases, individual blocks of analyses were bracketed by (and interspersed with) analyses of the same standard glasses as monitors of IMF drift within blocks and IMF offsets between blocks. We found that the relative gains of the electron multipliers used to collect ^{32}S and ^{34}S are one of the most important variables controlling the IMF factor. The reproducibility of the standard after drift and IMF corrections was 0.9‰ (2σ, n = 31) (fig. S5B). The accuracy of δ^{34}S for this standard is 0.8‰ (2σ), producing a combined total uncertainty of ~1.2‰ (2σ). The measured ratios were then normalized to a $^{34}S/^{32}S$ ratio of 0.0441626 for V-CDT (74) to calculate δ^{34}S values for each analysis.

Scanning ion imaging

In this mode of operation, the instrument was used in an identical fashion as with dynamic SIMS, except that the sputter crater was divided into regions of 256 × 256 pixels. Beam blanking was not used. Data were recorded as scanning ion images obtained simultaneously on each mass (^{12}C, ^{18}O, ^{32}S, ^{34}S); in this mode, acquisition of a single

frame takes ~16 s and 40 frames were acquired at each analysis location, resulting in a total acquisition time of ~10 min. Data were extracted and processed from the ion images using the L'Image software package for PV Wave written by L. Nittler (Carnegie institution for Science). Data were first corrected for system dead time, and the last 36 images were summed (the first four images were used as a pre-sputter). The images were ratioed to produce scanning isotope ratio images ($^{34}S/^{32}S$), and data were extracted from specific regions of interest (ROIs) located within the isotope ratio images. Each ROI consisted of a user-defined region that enclosed the entire melt inclusion without overlap onto surrounding olivine, daughter crystals (ilmenite), or vapor bubbles and without overlapping areas near the edge of the sputter crater containing surface contamination of volatiles (fig. S6). For isotope ratio images of melt inclusions, the NanoSIMS sample stage was adjusted so that the inclusion was centered in the sputter crater before pre-sputtering and image acquisition. Measured sulfur isotope ratios were corrected for the long-term analytical drift of the instrumental fractionation using a time-based linear interpolation of all $^{34}S/^{32}S$ values of the ALV892-1 standard (23, 44, 72) within each analytical session (fig. S7A). The in-run precision for the melt inclusions was 0.8 to 0.9‰ (2σ). We interspersed analyses of the basaltic glass standard between every two or three analyses of lunar melt inclusions to monitor the IMF of sulfur isotopes. For images of standard, ROIs were located in the center of the image. Average count rates per ROI on standard ALV892-1 glass (1606-ppm S) were 3.66 × 10^8 for ^{32}S and 1.64 × 10^7 for ^{34}S. The IMF factor measured during the single session for melt inclusion analyses was 1.014. The δ^{34}S reproducibility of the standard after drift and IMF corrections was 0.86‰ (2σ, n = 12) (fig. S7B) and the accuracy was 0.5‰ (2σ), producing a combined total uncertainty of ~1 ‰ (2σ).

SUPPLEMENTARY MATERIALS

REFERENCES AND NOTES

1. C. K. Shearer, P. C. Hess, M. A. Wieczorek, M. E. Pritchard, E. M. Parmentier, L. E. Borg, J. Longhi, L. T. Elkins-Tanton, C. R. Neal, I. Antonenko, R. M. Canup, A. N. Halliday, T. L. Grove, B. H. Hager, D.-C. Lee, U. Wiechert, Thermal and magmatic evolution of the Moon. *Rev. Mineral. Geochem.* **60**, 365–518 (2006).
2. B. A. Wing, J. Farquhar, Sulfur isotope homogeneity of lunar mare basalts. *Geochim. Cosmochim. Acta* **170**, 266–280 (2015).
3. H. G. Thode, C. E. Rees, Sulphur isotopes in grain size fractions of lunar soils. *Proc. Lunar Sci. Conf.* **7**, 459–468 (1976).
4. T. P. Ding, H. G. Thode, C. E. Rees, Sulphur content and sulphur isotope composition of orange and black glasses in Apollo 17 drive tube 74002/1. *Geochim. Cosmochim. Acta* **47**, 491–496 (1983).
5. E. K. Gibson Jr., R. Brett, F. Andrawes, Sulfur in lunar mare basalts as a function of bulk composition. *Proc. Lunar Sci. Conf.* **8**, 1417–1428 (1977).
6. D. J. Des Marias, Light element geochemistry and spallogenesis in lunar rocks. *Geochim. Cosmochim. Acta* **47**, 1769–1781 (1983).
7. I. R. Kaplan, J. W. Smith, E. Ruth, Carbon and sulfur concentration and isotopic composition in Apollo 11 lunar samples. *Proc. Lunar Sci. Conf.* **11**, 1317–1329 (1970).
8. I. R. Kaplan, J. F. Kerridge, C. Petrowski, Light element geochemistry of the Apollo 15 site. *Proc. Lunar Sci. Conf.* **7**, 481–492 (1976).
9. I. R. Kaplan, C. Petrowski, Carbon and sulfur isotope studies on Apollo 12 lunar samples. *Proc. Lunar Sci. Conf.* **2**, 1397–1406 (1971).
10. H. G. Thode, C. E. Rees, Measurement of sulphur concentrations and the isotope ratios33S/32S, $^{34}S/^{32}S$ and36S/32S in Apollo 12 samples. *Earth Planet. Sci. Lett.* **12**, 434–438 (1971).
11. C. E. Rees, H. G. Thode, Sulphur concentrations and isotope ratios in lunar samples. *Proc. Lunar Sci. Conf.* **3**, 1479–1485 (1972).
12. C. E. Rees, H. G. Thode, Sulfur concentrations and isotope ratios in Apollo 16 and 17 samples. *Proc. Lunar Sci. Conf.* **5**, 1963–1973 (1974).

13. S. Chang, K. Lennon, E. K. Gibson Jr., Abundances of C, N, H, He, and S in Apollo 17 soils from Station 3 and 4: Implications for solar wind exposure ages and regolith evolution. *Proc. Lunar Sci. Conf.* **5**, 1785–1800 (1974).

14. C. Petrowski, J. F. Kerridge, I. R. Kaplan, Light element geochemistry of the Apollo 17 site. *Proc. Lunar Sci. Conf.* **5**, 1939–1948 (1974).

15. E. K. Gibson Jr., S. Chang, K. Lennon, G. W. Moore, G. W. Pearce, Sulfur abundances and distributions in mare basalts and their source magmas. *Proc. Lunar Sci. Conf.* **6**, 1287–1301 (1975).

16. J. F. Kerridge, I. R. Kaplan, C. Petrowski, Evidence for meteoritic sulfur in the lunar regolith. *Proc. Lunar Sci. Conf.* **6**, 2151–2162 (1975).

17. J. F. Kerridge, I. R. Kaplan, C. Petrowski, S. Chang, Light element geochemistry of the Apollo 16 site. *Geochim. Cosmochim. Acta* **39**, 137–162 (1975).

18. J. F. Kerridge, I. R. Kaplan, C. C. Kung, D. A. Winter, D. L. Friedman, Light element geochemistry of the Apollo 12 site. *Geochim. Cosmochim. Acta* **42**, 391–402 (1978).

19. E. K. Gibson Jr., G. W. Moore, Carbon and sulfur distributions and abundances in lunar fines. *Proc. Lunar Sci. Conf.* **4**, 1577–1586 (1973).

20. J. W. Delano, B. Z. Hanson, E. B. Watson, Abundance and diffusion of sulfur in lunar picritic magmas. *Proc. Lunar Sci. Conf.* **25**, 325–326 (1994).

21. R. N. Clayton, T. K. Mayeda, J. M. Hurd, Loss of oxygen, silicon, sulfur and potassium from the lunar regolith. *Proc. Lunar Sci. Conf.* **5**, 1801–1808 (1974).

22. J. Labidi, P. Cartigny, M. Moreira, Non-chondritic sulphur isotope composition of the terrestrial mantle. *Nature* **501**, 208–211 (2013).

23. A. Fiege, F. Holtz, N. Shimizu, C. W. Mandeville, H. Behrens, J. L. Knipping, Sulfur isotope fractionation between fluid and andesitic melt: An experimental study. *Geochim. Cosmochim. Acta* **142**, 501–521 (2014).

24. A. E. Saal, E. H. Hauri, M. Lo Cascio, J. A. Van Orman, M. C. Rutherford, R. Cooper, Volatile content of lunar volcanic glasses and the presence of water in the Moon's interior. *Nature* **454**, 192–195 (2008).

25. E. H. Hauri, T. Weinreich, A. E. Saal, M. C. Rutherford, J. A. Van Orman, High pre-eruptive water contents preserved in lunar melt inclusions. *Science* **333**, 213–215 (2011).

26. A. E. Saal, E. H. Hauri, J. A. Van Orman, M. J. Rutherford, Hydrogen isotopes in lunar volcanic glasses and melt inclusions reveal a carbonaceous chondrite heritage. *Science* **340**, 1317–1320 (2013).

27. E. H. Hauri, A. E. Saal, M. J. Rutherford, J. A. Van Orman, Water in the Moon's interior: Truth and consequences. *Earth Planet. Sci. Lett.* **409**, 252–264 (2015).

28. D. T. Wetzel, E. H. Hauri, A. E. Saal, M. J. Rutherford, Carbon content and degassing history of the lunar volcanic glasses. *Nat. Geosci.* **8**, 755–758 (2015).

29. J. W. Delano, Apollo 15 green glass—Chemistry and possible origin. *Proc. Lunar Sci. Conf.* **10**, 275–300 (1979).

30. L. T. Elkins-Tanton, N. Chatterjee, T. L. Grove, Experimental and petrological constraints on lunar differentiation from the Apollo 15 green picritic glasses. *Meteorit. Planet. Sci.* **38**, 515–527 (2003).

31. K. Hashizume, M. Chaussidon, B. Marty, F. Robert, Solar wind record on the Moon: Deciphering presolar from planetary nitrogen. *Science* **290**, 1142–1145 (2000).

32. E. S. Steenstra, A. X. Seegers, J. Eising, B. G. J. Tomassen, F. P. F. Webers, J. Berndt, S. Klemme, S. Matveev, W. van Westrenen, Evidence for a sulfur-undersaturated lunar interior from the solubility of sulfur in lunar melts and sulfide-silicate partitioning of siderophile elements. *Geochim. Cosmochim. Acta* **231**, 130–156 (2018).

33. S. Ding, T. Hough, R. Dasgupta, New high pressure experiments on sulfide saturation of high-FeO* basalts with variable TiO₂ contents - Implications for the sulfur inventory of the lunar interior. *Geochim. Cosmochim. Acta* **222**, 319–339 (2018).

34. E. S. Steenstra, J. Berndt, S. Klemme, J. F. Snape, E. S. Bullock, W. van Westrenen, The fate of sulfur and chalcophile elements during crystallization of the lunar magma ocean. *J. Geophys. Res. Planets* **125**, e2019JE006328 (2020).

35. J. M. Brenan, J. E. Mungall, N. R. Bennett, Abundance of highly siderophile elements in lunar basalts controlled by iron sulfide melt. *Nat. Geosci.* **12**, 701–706 (2019).

36. J. W. Delano, Pristine lunar glasses: Criteria, data, and implications. *Proc. Lunar Planet. Sci. Conf.* **16**, 201–213 (1986).

37. S. S. Hughes, J. W. Delano, R. A. Schmitt, Apollo 15 yellow-brown volcanic glass: Chemistry and petrogenetic relations to green volcanic glass and olivine-normative mare basalts. *Geochim. Cosmochim. Acta* **52**, 2379–2391 (1988).

38. S. S. Hughes, J. W. Delano, R. A. Schmitt, Petrogenetic modeling of 74220 high-Ti orange volcanic glasses and the Apollo11 and 17 high-Ti mare basalts. *Proc. Lunar Planet. Sci. Conf.* **19**, 175–188 (1989).

39. D. J. Bombardieri, M. D. Norman, V. S. Kamenetsky, L. V. Danyushevsky, Major element and primary sulfur concentrations in Apollo 12 mare basalts: The view from melt inclusions. *Meteorit. Planet. Sci.* **40**, 679–693 (2005).

40. P. J. Jugo, M. Wilke, R. E. Botcharnikov, Sulfur K-edge XANES analysis of natural and synthetic basaltic glasses: Implications for S speciation and S content as function of oxygen fugacity. *Geochim. Cosmochim. Acta* **74**, 5926–5938 (2010).

41. L. Marini, R. Moretti, M. Accornero, Sulfur isotopes in magmatic-hydrothermal systems, melts, and magmas. *Rev. Mineral. Geochem.* **73**, 423–492 (2011).

42. L. Wilson, J. W. Head III, Controls on lunar basaltic volcanic erupton structure and morphology: Gas release patterns in sequential eruption phases. *Geophys. Res. Lett.* **45**, 5852–5859 (2018).

43. Apollo 15 Preliminary Examination Team, The Apollo 15 lunar samples: A preliminary description. *Science* **175**, 363–375 (1972).

44. A. Fiege, F. Holtz, H. Behrens, C. W. Mandeville, N. Shimizu, L. S. Crede, J. Göttlicher, Experimental investigation of the S and S-isotope distribution between H₂O-S ± Cl fluids and basaltic melts during decompression. *Chem. Geol.* **393-394**, 36–54 (2015).

45. C. J. Renggli, P. L. King, R. W. Henley, M. D. Norman, Volcanic gas composition, metal dispersion and deposition during explosive volcanic eruptions on the Moon. *Geochim. Cosmochim. Acta* **206**, 296–311 (2017).

46. J. M. Watkins, D. J. DePaolo, F. J. Ryerson, B. T. Peterson, Influence of liquid structure on diffusive isotope separation in molten silicates and aqueous solutions. *Geochim. Cosmochim. Acta* **75**, 3103–3118 (2011).

47. G. Goel, L. Zhang, D. J. Lacks, J. A. Van Orman, Isotope fractionation by diffusion in silicate melts: Insights from molecular dynamics simulations. *Geochim. Cosmochim. Acta* **93**, 205–213 (2012).

48. Y. Zhang, H. Ni, Y. Chen, Diffusion data in silicate melts. *Rev. Mineral. Geochem.* **72**, 171–225 (2010).

49. Z. Morgan, Y. Liang, P. Hess, An experimental study of anorthosite dissolution in lunar picritic magmas: Implications for crustal assimilation processes. *Geochim. Cosmochim. Acta* **70**, 3477–3491 (2006).

50. M.-A. Fortin, E. B. Watson, R. A. Stern, S. Ono, Experimental characterization of diffusive and Soret isotopic fractionation of sulfur in a reduced, anhydrous basaltic melt. *Chem. Geol.* **510**, 10–17 (2019).

51. A. M. Davis, F. M. Richter, Condensation and evaporation of solar system materials, in *Treatise on Geochemistry (Second Edition)* H. D. Holland and K. K. Turekian, Eds. **1**, 335–360 (2014).

52. N. Dauphas, F. Poitrasson, C. Burkhardt, H. Kobayashi, K. Kurosawa, Planetary and meteoritic Mg/Si and δ³⁰Si variations inherited from solar nebula chemistry. *Earth Planet. Sci. Lett.* **427**, 236–248 (2015).

53. C. Ma, Y. Liu, Discovery of a zinc-rich mineral on the surface of lunar orange pyroclastic beads. *Am. Mineral.* **104**, 447–452 (2019).

54. V. Viswanathan, N. Rambaux, A. Fienga, J. Laskar, M. Gastineau, Observational constraint on the radius and oblateness of the lunar core-mantle boundary. *Geophys. Res. Lett.* **46**, 7295–7303 (2018).

55. E. S. Steenstra, N. Rai, J. S. Knibbe, Y. H. Lin, W. van Westrenen, New geochemical models of core formation in the Moon from metal-silicate partitioning of 15 siderophile elements. *Earth Planet. Sci. Lett.* **441**, 1–9 (2016).

56. K. Righter, Volatile element depletion of the Moon: The roles of precursors, post-impact disk dynamics, and core formation. *Sci. Adv.* **5**, eaau7658 (2019).

57. W. F. McDonough, S.-S. Sun, The composition of the Earth. *Chem. Geol.* **120**, 223–253 (1995).

58. E. S. Steenstra, Y. H. Lin, D. Dankers, N. Rai, J. Berndt, S. Matveev, W. van Westrenen, Metal-silicate partitioning of S, Se, Te and Sb suggests minor volatile loss during lunar formation and no volatile-rich late veneer. *Proc. Lunar Sci. Conf.* **48**, Abstract 1051 (2017).

59. A. Boujibar, D. Andrault, M. A. Bouhifda, N. Bolfan-Casanova, J.-L. Devidal, N. Trcera, Metal silicate partitioning of sulphur, new experimental and thermodynamic constraints on planetary accretion. *Earth Planet. Sci. Lett.* **391**, 42–54 (2014).

60. A. Shahar, Y. Fei, M. C. Liu, J. Wang, Sulfur isotopic fractionation during Mars differentiation. *Goldschmidt Conf.* Abstract A1201 (2009).

61. J. Labidi, A. Shahar, C. Le Losq, V. J. Hillgren, B. O. Mysen, J. Farquhar, Experimentally determined sulfur isotope fractionation between metal and silicate and implications for planetary differentiation. *Geochim. Cosmochim. Acta* **175**, 181–194 (2016).

62. P. H. Warren, J. T. Wasson, The origin of KREEP. *Rev. Geophys.* **17**, 73–88 (1979).

63. M. A. Wieczorek, G. A. Neumann, F. Nimmo, W. S. Kiefer, G. J. Taylor, H. J. Melosh, R. J. Phillips, S. C. Solomon, J. C. Andrews-Hanna, S. W. Asmar, A. S. Konopliv, F. G. Lemoine, D. E. Smith, M. M. Watkins, J. G. Williams, M. T. Zuber, The crust of the Moon as seen by GRAIL. *Science* **339**, 671–675 (2013).

64. B. Charlier, T. L. Grove, O. Namur, F. Holtz, Crystallization of the lunar magma ocean and the primordial mantle-crust differentiation of the Moon. *Geochim. Cosmochim. Acta* **234**, 50–69 (2018).

65. Z. D. Sharp, C. K. Shearer, K. D. McKeegan, J. D. Barnes, Y. Q. Wang, The chlorine isotope composition of the Moon and implications for an anhydrous mantle. *Science* **329**, 1050–1053 (2010).

66. C. Kato, F. Moynier, M. C. Valdes, J. K. Dhaliwal, J. M. D. Day, Extensive volatile loss during formation and differentiation of the Moon. *Nat. Commun.* **6**, 7617 (2015).

67. G. F. Herzog, F. Moynier, F. Albarede, A. A. Berezhnoy, Isotopic and elemental abundances of copper and zinc in lunar samples, Zagami, Pele's hairs, and a terrestrial basalt. *Geochim. Cosmochim. Acta* **73**, 5884–5904 (2009).

68. M. D. Norman, K. Keil, W. L. Griffin, C. G. Ryan, Fragments of ancient lunar crust: Petrology and geochemistry of ferroan noritic anorthosites from the Descartes region of the Moon. *Geochim. Cosmochim. Acta* **59**, 831–847 (1995).

69. C. K. Shearer, P. V. Burger, Y. Guan, J. J. Papike, S. R. Sutton, N. V. Atudorei, Origin of sulfide replacement textures in lunar breccias. Implications for vapor element transport in the lunar crust. *Geochim. Cosmochim. Acta* **83**, 138–158 (2012).

70. A. S. Bell, C. Shearer, J. M. deMoor, P. Provencio, Using the sulfide replacement petrology in lunar breccia 67915 to construct a thermodynamic model of S-bearing fluid in the lunar crust. *Geochim. Cosmochim. Acta* **171**, 50–60 (2015).

71. Y. Li, J. Liu, Calculation of sulfur isotope fractionation in sulfides. *Geochim. Cosmochim. Acta* **70**, 1789–1795 (2006).

72. C. W. Mandeville, N. Shimizu, K. A. Kelley, L. Cheek, Sulfur isotope variation in basaltic melt inclusions from Krakatau revealed by a newly developed secondary ion mass spectrometry technique for silicate glasses. *Eos. Trans. AGU* Abstract V13-F07 (2008).

73. B. A. Black, E. H. Hauri, L. T. Elkins-Tanton, S. M. Brown, Sulfur isotopic evidence for sources of volatiles in Siberian Traps magmas. *Earth Planet. Sci. Lett.* **394**, 58–69 (2014).

74. T. Ding, S. Valkiers, H. Kipphardt, P. De Bievre, P. D. P. Taylor, R. Gonfiantini, R. Krouse, Calibrated sulfur isotope abundance ratios of three IAEA sulfur isotope reference materials and V-CDT with a reassessment of the atomic weight of sulfur. *Geochim. Cosmochim. Acta* **65**, 2433–2437 (2001).

75. H. Ohmoto, R. O. Rye, Isotopes of sulfur and carbon, in *Geochemistry of Hydrothermal Ore Deposits*, H. L. Barnes, Ed. (Wiley, ed. 2, 1979), pp. 509–567.

76. P. Richet, Y. Bottinga, M. Javoy, A review of hydrogen, carbon, nitrogen, oxygen, sulphur, and chlorine stable isotope fractionation among gaseous molecules. *Annu. Rev. Earth Planet. Sci.* **5**, 65–110 (1977).

77. B. E. Taylor, Magmatic volatiles: Isotopic variation of C, H, and S. *Rev. Mineral. Geochem.* **16**, 185–225 (1986).

Citation: A. E. Saal, E. H. Hauri, Large sulfur isotope fractionation in lunar volcanic glasses reveals the magmatic differentiation and degassing of the Moon. *Sci. Adv.* **7**, eabe4641 (2021).